

Photoconductivity of biased graphene

Marcus Freitag^{*}, Tony Low, Fengnian Xia^{*} and Phaedon Avouris

Graphene is a promising candidate for optoelectronic applications such as photodetectors, terahertz imagers and plasmonic devices. The origin of the photoresponse in graphene junctions has been studied extensively and is attributed to either thermoelectric or photovoltaic effects. In addition, hot carrier transport and carrier multiplication are thought to play an important role. Here, we report the intrinsic photoresponse in biased but otherwise homogeneous graphene. In this classic photoconductivity experiment, the thermoelectric effects are insignificant. Instead, the photovoltaic and a photo-induced bolometric effect dominate the photoresponse. The measured photocurrent displays polarity reversal as it alternates between these two mechanisms in a backgate voltage sweep. Our analysis yields elevated electron and phonon temperatures, with the former an order higher than the latter, shedding light on the understanding of the hot electron-driven photoresponse in graphene and its energy loss pathway via phonons.

The optoelectronic properties of graphene have attracted substantial interest because of graphene's high carrier mobility, zero bandgap and electron–hole symmetry¹. Graphene can absorb light and convert it into a photocurrent over a wide range of the electromagnetic spectrum, from the ultraviolet to visible and infrared regimes. A photocurrent response at graphene–metal contacts has been reported by various groups, including ours^{2–5}, and in these early reports the origin of photocurrent generation was attributed to the classical photovoltaic effect. The thermoelectric Seebeck effect, induced through photo-excited carriers, was first identified in single-layer–bilayer graphene junction experiments as the origin of photocurrent⁶. The technologically important photocurrent in graphene p–n junctions has been described as either photovoltaic^{5,7} or thermoelectric^{8–10} in nature. Both mechanisms may be enhanced by the hot carriers^{11–16} that persist after photoexcitation in graphene due to an electron–acoustic phonon decay bottleneck^{9,13}. Electron–electron scattering, on the other hand, dominates photocarrier energy relaxation, where the energetic photoexcited carriers multiply while decaying towards an elevated electronic temperature T_E (refs 9,15). The decoupling of electron and lattice temperatures in graphene may also explain how thermoelectric contributions can be compatible with the fast photoresponse on the order of 100 GHz or more seen in modulated photocurrent measurements^{16–18}. Owing to the identical polarity of photovoltaic and thermoelectric currents in metal–graphene or graphene p–n junctions, it has been quite a challenge to identify the dominant photocurrent mechanism. However, the two effects show opposite polarity in the unipolar junction regimes pp^+ and nn^- , which allowed the identification of the thermoelectric effect in the photocurrent of graphene with boron nitride dielectrics¹⁰. Very recently, a bolometric photoresponse was observed in gapped bilayer graphene¹⁹ and in single-layer graphene with superconducting leads²⁰.

In this Article, we investigate the origins of the photocurrent response in biased graphene by measuring the photoconductivity of the homogeneous graphene channel in a graphene field-effect transistor (FET) fabricated on silicon/silicon oxide (Si/SiO₂). In this most simple and yet unstudied configuration, the photocurrent polarities due to photovoltaic and thermoelectric effects are opposite, allowing us to directly determine the dominant photocurrent generation mechanism at low electrostatic doping to be photovoltaic. The thermoelectric effect is calculated to be an order of

magnitude smaller. The photo-induced bolometric effect dominates in the n-type and p-type doping regimes.

The graphene FETs used in this work were biased at one contact with a moderate drain voltage on the order of $V_D = -1$ V. We defined a positive current as flowing from the source to the drain. Joule heating was estimated at ~ 10 K, which is small compared to the base temperatures of 300 K and 200 K in these experiments. The doping level in the graphene was controlled electrostatically by means of a global silicon backgate. While a chopped and focused laser beam at a wavelength of 690 nm was scanned over the sample, we measured the a.c. photocurrent amplitude and phase, which were obtained using a lock-in amplifier referenced to the chopping frequency (Fig. 1a). (For details of sample preparation and measurements see Methods.) Photocurrent images (Fig. 1c) show a uniform photocurrent within the interior of the graphene channel, exhibiting a photoresponse on the order of $2.5 \times 10^{-4} \text{ A W}^{-1}$. Contact effects, which have been discussed extensively for the zero bias case (Fig. 1b)^{2–6}, are limited to the immediate vicinity of the leads. Under applied bias, a small photocurrent ($\sim 10\%$ of the observed value at graphene) is also observed when the laser beam is positioned a few micrometres away from the graphene over the bare Si/SiO₂ substrate. The photocurrents from graphene and the substrate exhibit opposite signs at a gate voltage of $V_G = 5$ V, as can be seen in the phase image. We show in Supplementary Section SI that the substrate-related photocurrent arises as a result of a 2 mV photovoltage generated at the Si/SiO₂ interface that is sensed by the graphene FET. This 'photo field effect' switches sign when the Fermi level in the graphene is swept past the charge neutrality point. We can easily correct for its effect at the graphene position.

When photons are incident directly on the graphene channel, a true photocurrent from graphene ensues. This photocurrent switches sign twice when the Fermi level in the device is swept from p-type over intrinsic to n-type (Fig. 2a). Figure 2b,c shows the photocurrent in the centre of the graphene as a function of gate voltage. Between gate voltages $V_G = 0$ V and 2.3 V, the photocurrent peaks near the Dirac point, and points in the direction of the d.c. current (from source to drain). Outside this range, the photocurrent is negative. The largest photocurrent amplitude is reached at high electrostatic doping with either electrons or holes. Figure 3 shows the full gate and drain voltage dependence of the a.c. photocurrent near the centre of the device. The sixfold pattern observed in

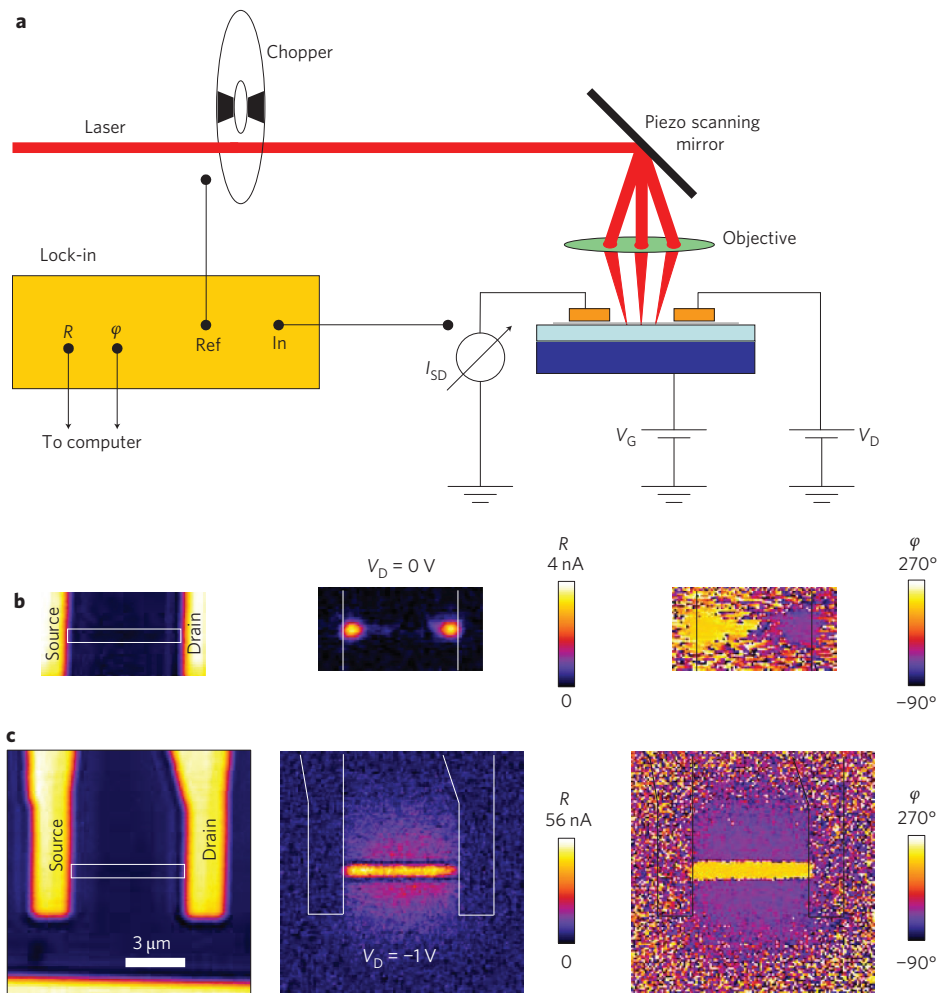


Figure 1 | Photoconductivity (a.c.) of graphene with and without bias. **a**, Schematic of the photoconductivity measurement set-up with a laser wavelength of $\lambda = 690$ nm, laser power of $P = 220 \mu\text{W}$, spot diameter of $d \approx 700$ nm, and chopping frequency of $f = 1.1$ kHz. **b**, Photocurrent (a.c.) at $V_D = 0$ V drain bias (short-circuit photocurrent) and $V_G = 5$ V gate bias (n-type regime). Left: the laser-scanning image shows the source and drain electrodes. The outline of the graphene sheet is indicated. Middle: amplitude R of the photocurrent. Right: phase φ of the photocurrent. A localized photocurrent is generated close to the contacts. The phases at source and drain contacts are $\varphi \approx 180^\circ$ (corresponding to negative I_{ph}) and $\varphi \approx 0^\circ$ (positive I_{ph}), respectively. **c**, Photocurrent (a.c.) under a drain bias of $V_D = -1$ V and gate voltage of $V_G = 5$ V. Laser scanning, amplitude and phase images are shown. The entire graphene channel is producing a photocurrent under applied bias, and the photocurrent is uniform in both amplitude ($R \approx 46$ nA) and phase ($\varphi \approx 180^\circ$) throughout the channel except for the contact regions. The small photocurrent generated next to the graphene channel is in response to a photovoltage at the Si/SiO₂ interface that couples capacitively to the graphene FET.

Fig. 3c is reminiscent of the situation in a dual-gated graphene p–n junction without source–drain bias^{9,10}, but its origin is completely different as we will see below. It is composed of a twofold sign change with gate voltage, and a single sign change with drain voltage. The systematic shift in the conduction minimum or Dirac point with drain voltage (Fig. 3a) is well understood as channel doping by the drain voltage. In the centre of the device this shift in Dirac point amounts to $V_D/2$. It leads to a tilt in the near-vertical lines that separate positive and negative photocurrent regions in Fig. 3c, and it manifests itself in the shift in peak photocurrent position in Fig. 3d. The peak photocurrent is thus always associated with the Dirac point voltage. A short-circuit photocurrent on the order of 16 nA is visible near charge neutrality in the $V_D = 0$ V case (Fig. 3d). It also contributes at other drain voltages as a result of residual doping (electron–hole puddles) induced by the fixed laser beam in the centre of the device, which was necessary when sweeping both gate and drain voltages. The residual doping is not observed when the laser beam is continually scanned as in Figs 1 and 2, and we have corrected for this unintentional

non-uniform doping in Fig. 3e, where we plot the peak photocurrents. The drain voltage dependence of the peak photocurrent is linear up to voltages on the order of 1 V, above which saturation sets in. Joule heating, which is negligible at $|V_D| = 1$ V, may play a role in the photocurrent saturation at high bias (Supplementary Section SIII).

Several processes of photocurrent generation contribute in biased graphene. The first is the thermoelectric Seebeck effect, in which the laser spot produces a temperature gradient in the device, which together with a doping asymmetry generates a thermoelectric current. Although unbiased homogeneous graphene is not expected to produce a thermoelectric current, the presence of an applied drain voltage renders the electrochemical potential spatially variable, and a thermoelectric effect should ensue even in homogeneous graphene. The second is the photovoltaic effect, where photo-excited electrons and holes are accelerated in opposite directions by an electric field. The carriers produce a photocurrent either by reaching the contacts while still hot or by establishing a local photovoltage within the focal area that drives the photocurrent through

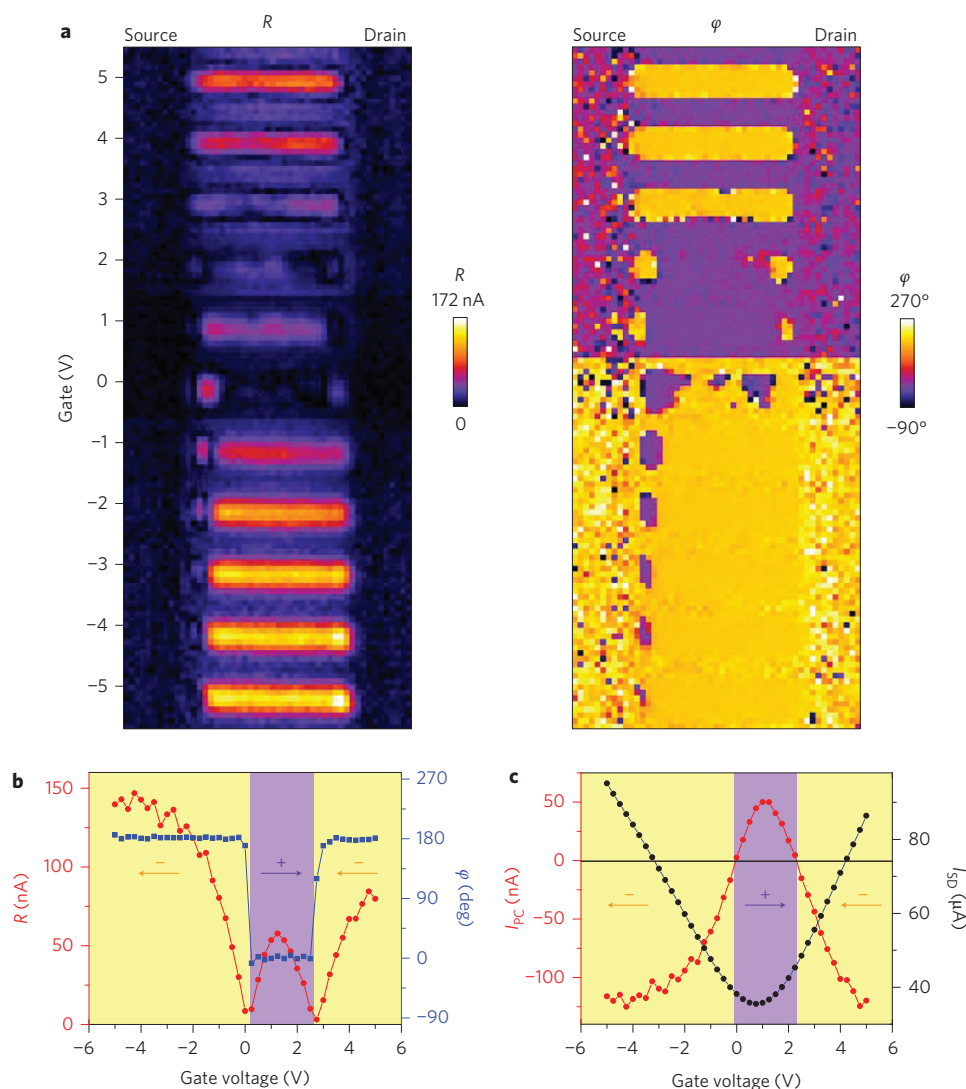


Figure 2 | Photocurrent (a.c.) as a function of gate voltage. **a**, Spatial images of the photocurrent amplitude and phase as a function of gate voltage (drain voltage $V_D = -1$ V; laser power $P = 370 \mu\text{W}$). The photocurrent in the graphene channel switches sign twice from negative ($\varphi \approx 180^\circ$) to positive ($\varphi \approx 0^\circ$) and back to negative ($\varphi \approx 180^\circ$). **b**, Photocurrent amplitude (red) and phase (blue) in the centre of the graphene channel as a function of gate voltage. The sign of the photocurrent is indicated. For comparison, the d.c. current flowing out of the source has positive sign for $V_D = -1$ V. **c**, Photocurrent (red) corrected for the photo field effect (Supplementary Section S1) and source-drain current (black) as a function of gate voltage.

the rest of the device⁸. The third is the bolometric effect, where the incident electromagnetic radiation raises the local temperature of the graphene, which alters the resistance of the device, producing a change in d.c. current under bias. Figure 4 summarizes the relative magnitude and signs of these effects in non-biased and biased graphene photodetectors. In the following we will discuss these effects in greater detail.

It is instructive to first review the thermoelectric effect in a p–n junction at zero bias^{6,8,10}. Figure 4a illustrates the experimental situation in a p–n junction, where the laser spot induces a temperature gradient dT/dx and results in a net thermoelectric voltage across the graphene due to the Seebeck effect. The generated photocurrent is proportional to $(S_2 - S_1)dT/dx$, where $S_{1/2}$ is the Seebeck coefficient for the two sides of the junction. The sign of the thermoelectric photocurrent is the same as that of the photovoltaic effect, except for in some unipolar junction regimes such as pp^+ or nn^- , where the thermoelectric current can be reversed¹⁰.

When the graphene doping is homogeneous, the photocurrent will be zero. However, the uniform doping can be rendered asymmetric under an applied drain bias, such that the effective doping

along the graphene channel changes gradually. This doping asymmetry and the associated Seebeck effect are more prominent at low doping. Typical energy band profiles are illustrated in Fig. 4b,c together with the sign of the various photocurrents relevant in our experiments. Figure 4d illustrates the respective biasing conditions. Near the charge neutrality point, the thermoelectric effect registers a photocurrent opposite in sign to both the experimentally measured photocurrent and the expected photovoltaic current. This makes it possible to directly differentiate between the thermoelectric and photovoltaic effects near the Dirac point. Because the Seebeck coefficient S is related to the electrical conductivity σ via the Mott formula

$$S = -\frac{\pi^2 k_B^2 T}{3e} \frac{1}{\sigma} \frac{d\sigma}{d\varepsilon}$$

application of thermoelectric theory yields an estimate of a thermoelectric photocurrent of ~ 4 nA near the Dirac point (Supplementary Section SV), opposite and an order of magnitude

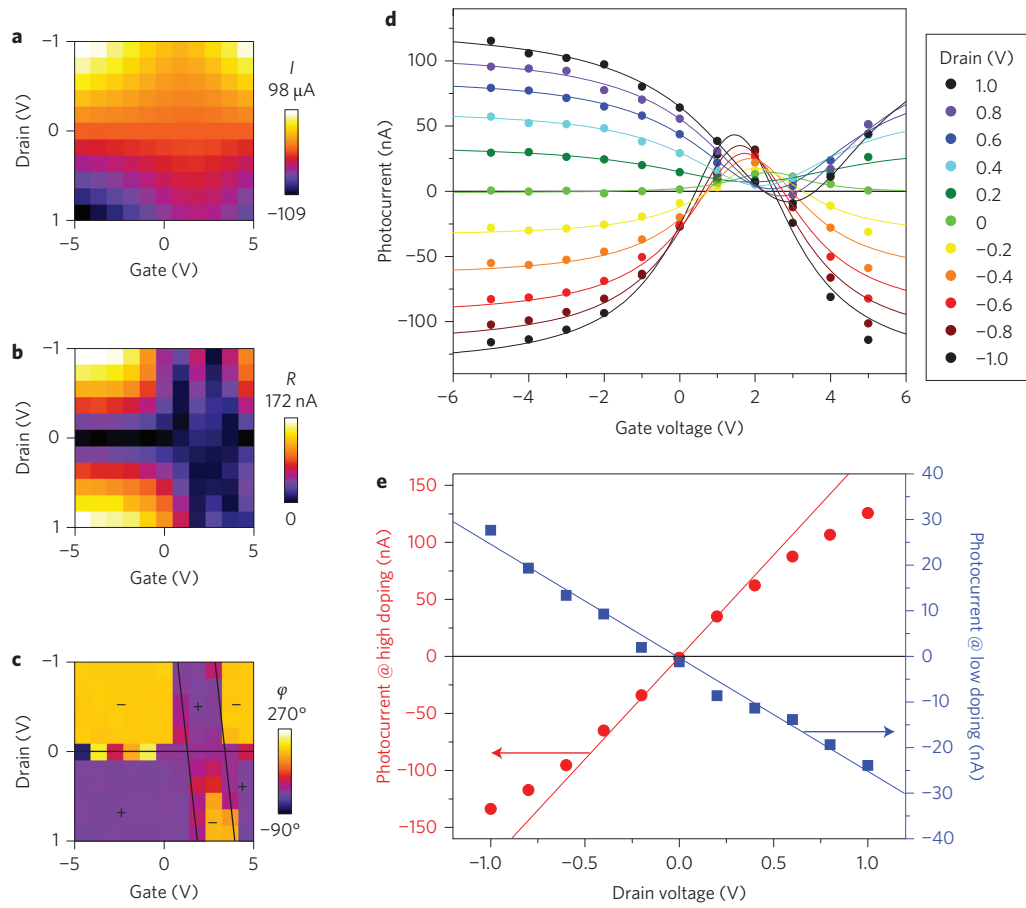


Figure 3 | Gate and drain voltage dependence of the photocurrent in the centre of the graphene detector. a–c, Current (d.c., **a**), photocurrent amplitude (**b**) and photocurrent phase (**c**) as a function of gate and drain voltages. Solid lines in **c** indicate the modelled sign change. **d,** Gate voltage characteristics of the photocurrent for different drain voltages, corrected for the photo field effect. Solid lines are Lorentzian fits to the data. **e,** Peak bias-induced photocurrents at high and low electrostatic doping as a function of drain voltage (solid lines are a guide to the eye). The photocurrent at high doping is due to the bolometric effect, while the photocurrent at low doping is due to the photovoltaic effect.

smaller than that observed in experiments. Away from the Dirac point, the thermoelectric effect is expected to be even less important because the electrochemical potential asymmetry is reduced with increasing Fermi level.

We next consider the bolometric response of the graphene photodetector, which can only be observed in biased devices and was therefore absent in previous short-circuit measurements on graphene contacts or junctions^{2–10}. The bolometric effect can be determined by measurement of the temperature dependence of the transport current. Figure 5a shows the change in transport current ΔI compared to its room-temperature value when cooling down in the cryostat. From this we can extract the gate voltage-dependent bolometric coefficient $\beta(V_G) = \Delta I(V_G)/\Delta T(V_G)$ (Fig. 5b, red curve), which describes the sensitivity of the transport current I to changes in temperature T around room temperature^{21–23}. A similar measurement around our lowest temperature of $T_0 = 205$ K yields the other (blue) curve for the temperature coefficient in Fig. 5b. The negative values of $\beta(V_G)$ in single-layer graphene are due to electron–acoustic phonon scattering and electron–remote phonon scattering of surface polar phonons in the SiO₂ underlayer, both of which are enhanced at elevated temperatures²¹. For comparison, Fig. 5c shows the experimental photocurrents at room temperature and $T_0 = 205$ K. The similar shapes of the curves in Fig. 5b,c are striking. In particular, both the bolometric coefficient and the photocurrent are largest (and negative) at high doping and the electron–hole asymmetry of the temperature coefficient is reproduced in the photocurrent measurement. Although the bolometric effect can

explain these general features of the gate voltage dependence of the photocurrent, it cannot explain the positive photocurrent in the direction of the d.c. current under conditions of low doping.

The photovoltaic effect is the only known mechanism that is consistent with the positive photoresponse near the Dirac point seen experimentally. Under light excitation, the hot carriers with separated electron and hole chemical potentials are formed on a timescale of the order of 100 fs, followed by a slow picosecond carrier recombination and cooling^{11–15,17}. At steady state, the photo-induced carrier density $n_{e/h}^*$ depends on its non-equilibrium carrier temperature T_e and the chemical potential and has to be determined by imposing charge conservation, that is, $n_e^* = n_h^*$. In addition, T_e has its maximum at the focal spot and is proportional to $\dot{Q}L/\kappa_0$, where \dot{Q} is the laser power, L is the device length, and κ_0 is the electronic thermal conductivity (related to the electronic conductivity through the Wiedemann–Franz relation). Making use of the above facts allows us to compute the gate-dependent photo-induced carrier densities $n_{e/h}^*(V_G)$ (Supplementary Section SVI). The photovoltaic current can then be estimated from $qn^*\mu\xi$, where ξ is the electric field and $\mu \approx 2,700$ cm² V⁻¹ s⁻¹ is the carrier mobility of our device. In general, the non-equilibrium $n_{e/h}^*$ values decrease with increasing equilibrium doping, consistent with electron–electron scattering, which increases with doping. Hence, the modelled photovoltaic current as shown in Fig. 5c decreases gradually with increasing bias away from the charge neutrality point. Near the Dirac point, the elevated electron temperatures are $T_E = T_e - T_0 \approx 8$ K and 12 K at initial temperatures $T_0 = 300$ K

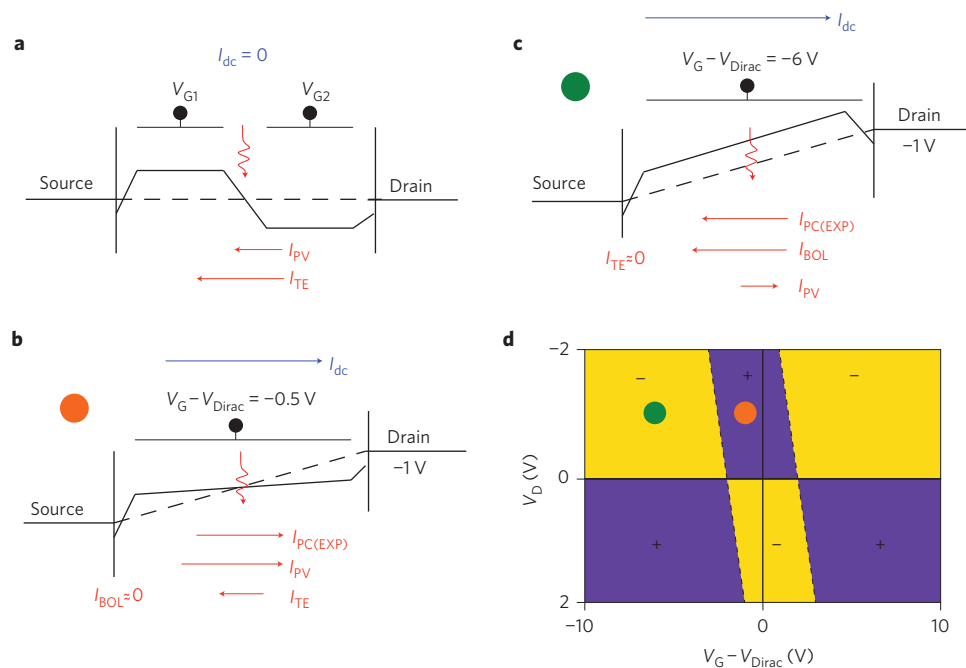


Figure 4 | Thermoelectric, bolometric and photovoltaic components of the graphene photocurrent. **a**, Energy band diagram of a graphene p–n junction used in typical photocurrent experiments, with laser incident at the junction interface. The d.c. current and thus the bolometric current are zero. Thermoelectric and photovoltaic components point in the same direction. **b,c**, Energy band diagrams for our experiments, where a uniform graphene channel is subjected to a finite source–drain bias V_D , under small and large electrostatic doping conditions, respectively. The thermoelectric (TE) and photovoltaic (PV) components are opposite, allowing for an unambiguous identification of the photocurrent (PC) generation mechanism. At low electrostatic doping the photovoltaic effect dominates, while at high electrostatic doping the bolometric (BOL) effect overshadows both photovoltaic and thermoelectric effects. **d**, Schematic diagram of the photocurrent direction with conditions **b** and **c** indicated by orange and green circles, respectively.

and 200 K, respectively, as shown in Fig. 5d; these also decrease with increasing equilibrium doping. The estimated electronic temperatures are lower bounds, because we neglect the small thermolectric component of the photocurrent, which points in the opposite direction.

We next subtract the estimated photovoltaic current component from our experimentally measured photocurrent to obtain the purely bolometric contribution I_{BOL} . The elevated lattice temperature $T_L = T_{\text{ph}} - T_0$ can then be determined from the ratio I_{BOL}/β , where β is the experimentally determined bolometric coefficient (Fig. 5b) discussed earlier. As shown in Fig. 5d, T_L is of the order of 1 K and is weakly dependent on doping. Both T_L and T_E are enhanced at lower temperatures as a result of less efficient heat flow. Although electron–electron interactions result in energy equilibration of the electronic system, they do not lead to a net energy loss. The dominant energy loss pathways are due to phonons. Intrinsic energy loss channels due to acoustic/optical phonons are known to be inefficient energy loss pathways and have a power density of only $Q_l \approx 10^5\text{--}10^4 \text{ W m}^{-2}$ for $T_E - T_L = 10 \text{ K}$ (Supplementary Section SVII)^{13,24}. However, with a typical graphene–substrate thermal resistance of $r_{\text{sg}} \approx 1 \times 10^{-7} \text{ km}^2 \text{ W}^{-1}$ (refs 25,26), our measured lattice temperature suggests a lattice heating power density of the order of $Q_l = T_L/r_{\text{sg}} \approx 1 \times 10^7 \text{ W m}^{-2}$ or somewhat lower, because of the uncertainty in the temperature at the Si/SiO₂ interface after photoexcitation. The inferred larger power density in experiments may indicate the presence of more efficient electron energy loss pathways in graphene devices. Electron–remote phonon scattering of surface polar phonons in the SiO₂ underlayer^{21,27–30}, and extrinsically enhanced graphene phonon-scattering processes mediated by ionized impurity and random strain-induced gauge fields³¹, may provide these additional decay pathways. More systematic studies in this regard are needed to clearly identify the energy dissipation mechanisms in graphene, but

it is clear from our measurements, that lattice heating is more efficient than expected from refs 9,10, even though electrons are a factor of 10 hotter than the lattice.

The responsivity of our graphene photodetector (on the order of $2.5 \times 10^{-4} \text{ A W}^{-1}$ for 1 V bias) is on par with those reported for graphene p–n junctions^{5,7–10}. However, because the entire graphene channel is photosensitive, our device offers real-world advantages. In addition, several techniques to enhance graphene photodetection have been reported within the last year. First, photodetection in single-layer graphene is mainly limited by the small light absorption coefficient of a few percent. However, plasmonic structures can greatly enhance the absorption coefficient, approaching total light absorption³². Indeed, advances in this direction have recently been demonstrated^{33,34}. Second, single-layer graphene has a limited temperature dependence due to the vanishing bandgap. The temperature sensitivity can be enhanced by either opening a bandgap in bilayer graphene, or by utilizing superconducting contacts that act as tunnel junctions. Two papers detailing these approaches have just been posted^{19,20}. These recent developments clearly demonstrate the rapid advancement in the optoelectronics device technology arena and the potentials for significant device improvements.

In conclusion, our measurement and theory of the intrinsic photoconductivity of biased graphene show that both bolometric and photovoltaic effects are relevant, and we have demonstrated in detail that operating conditions determine which photocurrent generation mechanism becomes dominant in graphene. The polarity and magnitude of the photocurrent can be modulated by electrostatic doping, which upon examination allows us to probe the non-equilibrium hot carrier and phonon characteristics. Our work therefore opens up the possibility of engineering the hot carrier photoresponse, which plays an essential role in applications such as bolometers, calorimeters and photodetectors.

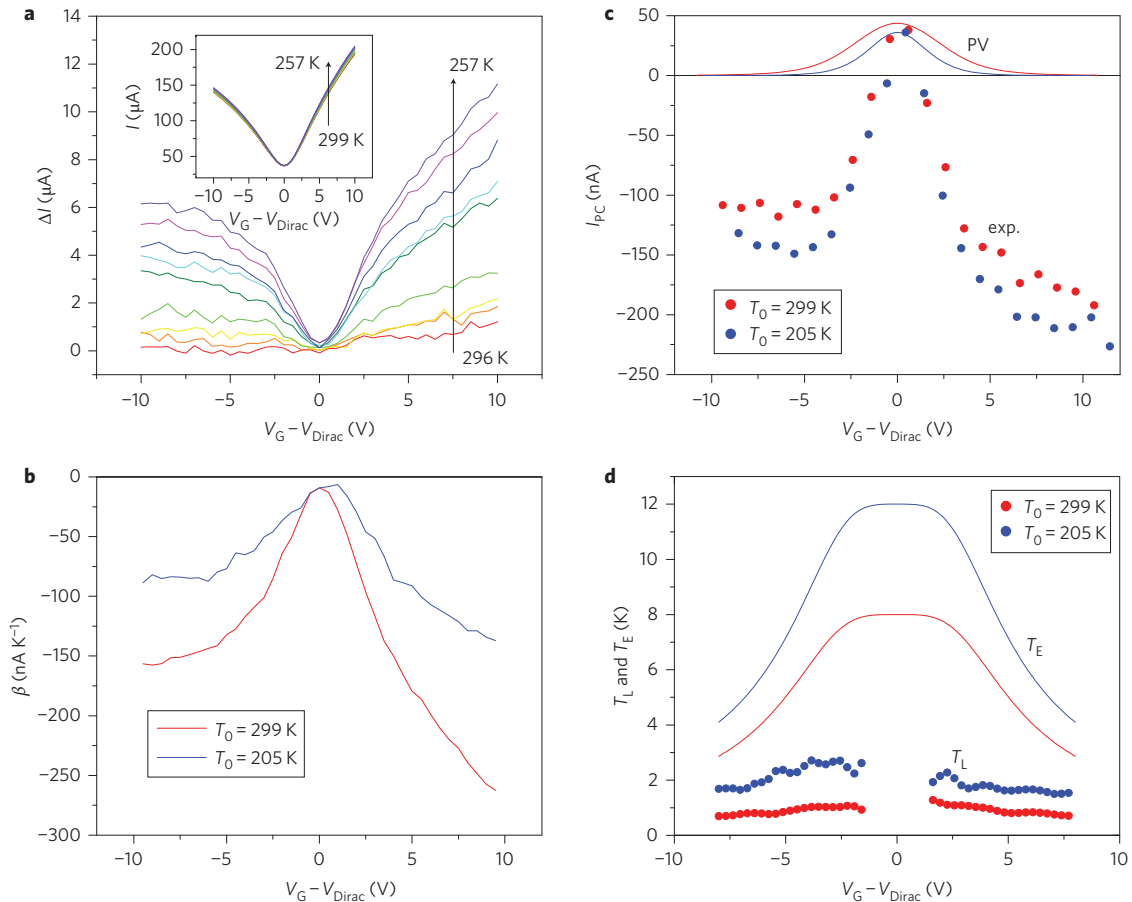


Figure 5 | Magnitude of bolometric and photovoltaic effects and determination of the hot electron and lattice temperatures. **a**, Temperature-dependent change in current from its room temperature ($T_0 = 299$ K) value as a function of gate voltage. Inset: gate voltage characteristic as a function of temperature when cooling down from room temperature. **b**, Bolometric coefficient $\beta(V_G) = \Delta I(V_G)/\Delta T(V_G)$ of the transport current as a function of gate voltage at two different ambient temperatures T_0 . **c**, Experimental photocurrent (PC, corrected for the photo field effect) and modelled photovoltaic component of the photocurrent. The photovoltaic (PV) component is important only near charge neutrality where it determines the sign of the overall photocurrent. Away from the Dirac point, the bolometric effect (**b**) dominates. **d**, Electron (T_E) and lattice (T_L) temperatures extracted from the data as detailed in the text.

Methods

Graphene FETs were fabricated by mechanical exfoliation from graphite. Electron-beam lithography and evaporation of 15 nm/70 nm of titanium/gold were used to create the contacts. A second electron-beam lithography step and plasma etching defined rectangular graphene sheets (length, 6 μm ; width, 1 μm). Single-layer graphene was identified by its optical contrast on the 90 nm SiO_2 dielectric. We used a highly doped (n-type) silicon substrate to avoid an excessive photo field effect, which dominates measurements on samples fabricated on lightly doped silicon. The as-prepared samples behaved in a p-type manner. To render them intrinsic, enhance mobility and reduce hysteresis, the samples were evacuated for a few days before the measurements and subjected to a combination of current annealing and laser scanning with a green laser for an hour. After this treatment, the Dirac point was near $V_G = 0$ V. The a.c. photoconductivity measurements were performed with a Ti:sapphire infrared laser at a wavelength of $\lambda \approx 690$ nm. The laser spot diameter on the sample was $d \approx 700$ nm. Incident laser power values are given in the figure captions. Considering the electric-field enhancement due to the gate stack, we estimate that 2.5% of the incident light was absorbed in the graphene. The photocurrent amplitudes reported in this Article are peak-to-peak values throughout. We confirmed that the chopping frequency $f = 1.1$ kHz was not too large by comparing our a.c. photocurrent results with equivalent d.c. measurements, which have much worse signal-to-noise ratio but agree with the photocurrent phase and amplitude reported in this Article. The photocurrent measurements were performed in an optical dewar with vacuum on the order of 1×10^{-5} to 1×10^{-6} torr, eliminating the effects of physisorption of oxygen³⁵ and allowing us to measure the temperature dependence.

Received 29 January 2012; accepted 9 November 2012;
published online 16 December 2012

References

- Bonaccorso, F., Sun, Z., Hasan, T. & Ferrari, A. C. Graphene photonics and optoelectronics. *Nature Photon.* **4**, 611–622 (2010).
- Lee, E. J. H., Balasubramanian, K., Weitz, R. T., Burghard, M. & Kern, K. Contact and edge effects in graphene devices. *Nature Nanotech.* **3**, 486–490 (2008).
- Mueller, T., Xia, F., Freitag, M., Tsang, J. & Avouris, P. Role of contacts in graphene transistors: a scanning photocurrent study. *Phys. Rev. B* **79**, 245430 (2009).
- Xia, F. *et al.* Photocurrent imaging and efficient photon detection in a graphene transistor. *Nano Lett.* **9**, 1039–1044 (2009).
- Peters, E. C., Lee, E. J., Burghard, M. & Kern, K. Gate dependent photocurrents at a graphene p–n junction. *Appl. Phys. Lett.* **97**, 193102 (2010).
- Xu, X., Gabor, N. M., Alden, J. S., van der Zande, A. M. & McEuen, P. L. Photo-thermoelectric effect at a graphene interface junction. *Nano Lett.* **10**, 562–566 (2009).
- Rao, G., Freitag, M., Chiu, H.-Y., Sundaram, R. S. & Avouris, P. Raman and photocurrent imaging of electrical stress-induced p–n junctions in graphene. *ACS Nano* **5**, 5848–5854 (2011).
- Lemme, M. C. *et al.* Gate-activated photoresponse in a graphene p–n junction. *Nano Lett.* **11**, 4134–4137 (2011).
- Song, J. C. W., Rudner, M. S., Marcus, C. M. & Levitov, L. S. Hot carrier transport and photocurrent response in graphene. *Nano Lett.* **11**, 4688–4692 (2011).
- Gabor, N. M. *et al.* Hot carrier-assisted intrinsic photoresponse in graphene. *Science* **334**, 648–652 (2011).
- George, P. A. *et al.* Ultrafast optical-pump terahertz-probe spectroscopy of the carrier relaxation and recombination dynamics in epitaxial graphene. *Nano Lett.* **8**, 4248–4251 (2008).

12. Sun, D. *et al.* Ultrafast relaxation of excited Dirac fermions in epitaxial graphene using optical differential transmission spectroscopy. *Phys. Rev. Lett.* **101**, 157402 (2008).
13. Bistritzer, R. & MacDonald, A. H. Electronic cooling in graphene. *Phys. Rev. Lett.* **102**, 206410 (2009).
14. Strait, J. H. *et al.* Very slow cooling dynamics of photoexcited carriers in graphene observed by optical-pump terahertz-probe spectroscopy. *Nano Lett.* **11**, 4902–4906 (2011).
15. Kim, R., Perebeinos, V. & Avouris, P. Relaxation of optically excited carriers in graphene. *Phys. Rev. B* **84**, 075449 (2011).
16. Sun, D. *et al.* Ultrafast hot-carrier-dominated photocurrent in graphene. *Nature Nanotech.* **7**, 114–118 (2012).
17. Urich, A., Unterrainer, K. & Mueller, T. Intrinsic response time of graphene photodetectors. *Nano Lett.* **11**, 2804–2808 (2011).
18. Xia, F., Mueller, T., Lin, Y.-M., Valdes-Garcia, A. & Avouris, P. Ultrafast graphene photodetector. *Nature Nanotech.* **4**, 839–843 (2009).
19. Yan, J. *et al.* Dual-gated bilayer graphene hot-electron bolometer. *Nature Nanotech.* **7**, 472–478 (2012).
20. Vora, H., Kumaravadivel, P., Nielsen, B. & Du, X. Bolometric response in graphene based superconducting tunnel junctions. *Appl. Phys. Lett.* **100**, 153507 (2012).
21. Chen, J.-H., Jang, C., Xiao, S., Ishigami, M. & Fuhrer, M. S. Intrinsic and extrinsic performance limits of graphene devices on SiO₂. *Nature Nanotech.* **3**, 206–209 (2008).
22. Zhu, W., Perebeinos, V., Freitag, M. & Avouris, P. Carrier scattering, mobilities, and electrostatic potential in monolayer, bilayer, and trilayer graphene. *Phys. Rev. B* **80**, 235402 (2009).
23. Efetov, D. K. & Kim, P. Controlling electron–phonon interactions in graphene at ultrahigh carrier densities. *Phys. Rev. Lett.* **105**, 256805 (2010).
24. Tse, W.-K. & Das Sarma, S. Energy relaxation of hot Dirac fermions in graphene. *Phys. Rev. B* **79**, 235406 (2009).
25. Freitag, M. *et al.* Energy dissipation in graphene field-effect transistors. *Nano Lett.* **9**, 1883–1888 (2009).
26. Koh, Y. K., Bae, M.-H., Cahill, D. G. & Pop, E. Heat conduction across monolayer and few-layer graphenes. *Nano Lett.* **10**, 4363–4368 (2010).
27. Meric, I. *et al.* Current saturation in zero-bandgap, top-gated graphene field-effect transistors. *Nature Nanotech.* **3**, 654–659 (2008).
28. Perebeinos, V., Rotkin, S. V., Petrov, A. G. & Avouris, P. The effects of substrate phonon mode scattering on transport in carbon nanotubes. *Nano Lett.* **9**, 312–316 (2008).
29. Rotkin, S. V., Perebeinos, V., Petrov, A. G. & Avouris, P. An essential mechanism of heat dissipation in carbon nanotube electronics. *Nano Lett.* **9**, 1850–1855 (2009).
30. Low, T., Perebeinos, V., Kim, R., Freitag, M. & Avouris, P. Cooling of photoexcited carriers in graphene by internal and substrate phonons. *Phys. Rev. B* **86**, 045413 (2012).
31. Song, J. C. W., Reizer, M. Y. & Levitov, L. S. Disorder-assisted electron–phonon scattering and cooling pathways in graphene. *Phys. Rev. Lett.* **109**, 106602 (2012).
32. Thongrattanasiri, S., Koppens, F. H. L. & Garcia de Abajo, F. J. Complete optical absorption in periodically patterned graphene. *Phys. Rev. Lett.* **108**, 047401 (2012).
33. Ju, L. *et al.* Graphene plasmonics for tunable terahertz metamaterials. *Nature Nanotech.* **6**, 630–634 (2011).
34. Yan, H. *et al.* Tunable infrared plasmonic devices using graphene/insulator stacks. *Nature Nanotech.* **7**, 330–334 (2012).
35. Shi, Y., Fang, W., Zhang, K., Zhang, W. & Li, L.-J. Photoelectrical response in single-layer graphene transistors. *Small* **5**, 2005–2011 (2009).

Acknowledgements

The authors thank B. Ek and J. Bucchignano for help with device fabrication and V. Perebeinos for discussions.

Author contributions

All authors discussed the results and commented on the manuscript.

Additional information

Supplementary information is available in the online version of the paper. Reprints and permission information is available online at <http://www.nature.com/reprints>. Correspondence and requests for materials should be addressed to M.F. and F.X.

Competing financial interests

The authors declare no competing financial interests.